



Multistability of segmented rings by programming natural curvature

Lu Lu^{a,1}, Sophie Leanza^{a,1}, Jize Dai^a, John W. Hutchinson^b, and Ruike Renee Zhao^{a,2}

Edited by John Rogers, Northwestern University, Evanston, IL; received March 20, 2024; accepted June 17, 2024

Multistable structures have widespread applications in the design of deployable aerospace systems, mechanical metamaterials, flexible electronics, and multimodal soft robotics due to their capability of shape reconfiguration between multiple stable states. Recently, the snap-folding of rings, often in the form of circles or polygons, has shown the capability of inducing diverse stable configurations. The natural curvature of the rod segment (curvature in its stress-free state) plays an important role in the elastic stability of these rings, determining the number and form of their stable configurations during folding. Here, we develop a general theoretical framework for the elastic stability analysis of segmented rings (e.g., polygons) based on an energy variational approach. Combining this framework with finite element simulations, we map out all planar stable configurations of various segmented rings and determine the natural curvature ranges of their multistable states. The theoretical and numerical results are validated through experiments, which demonstrate that a segmented ring with a rectangular cross-section can show up to six distinct planar stable states. The results also reveal that, by rationally designing the segment number and natural curvature of the segmented ring, its one- or multiloop configuration can store more strain energy than a circular ring of the same total length. We envision that the proposed strategy for achieving multistability in the current work will aid in the design of multifunctional, reconfigurable, and deployable structures.

multistability | structural instability | segmented rings | natural curvature

Multistability, the feature of elastic structures or solids having multiple stable equilibrium states, has recently emerged as a powerful platform used toward the design of shapereconfigurable architectures and aerospace structures (1-3), energy-trapping metamaterials (4, 5), flexible electronics (6, 7), and multimodal morphing robots (8–11). Under an external stimulus to overcome the energy barrier between stable states, a multistable structure transitions between its stable configurations for shape change and property tunability. Fig. 1A shows an example of the shape reconfiguration of a multisegment ring toy, which demonstrates the transitions from a planar configuration to three-dimensional (3D) architectures with tunable height. Among the various strategies to design functional multistable structures, one common method is to connect together multiple bistable units, such as curved beams and shells, which can be selectively actuated to switch between different stable states through structural instability (12–15). Recently, the snap-folding of rings has shown the capability of inducing diverse stable configurations with great area-tuning ability (16–19). These rings are often presented as circles, polygons, or their modified counterparts which can be folded into shapes with significantly reduced area and distinct morphology (18-22). In addition to the cross-sectional shape of the rod and geometry of the rings, the natural curvature of the rod segment (curvature in the stress-free state) plays an important role in the elastic stability of these rings, determining the number and form of their stable configurations during folding (23-30). Despite the elastic stability of rings having been studied by several works, most attention has been focused on circular rings (27-30), and the influence of natural curvature on the elastic stability of segmented rings (e.g., polygons) remains largely unexplored.

Recently, we have found that segmented rings exhibit intrinsically multistable configurations when their natural curvatures are rationally selected in coordination with the rod cross-sectional geometry. Fig. 1 B, i shows a rod segment as a building block of the multisegment ring. The rod of length L has a curvature κ_n in its stress-free state (referred to as the natural curvature) in the $(\mathbf{i}_1, \, \mathbf{i}_2)$ plane of the ring and a curvature κ_0 in the initially stressed state (referred to as the initial curvature). When connecting multiple identical rod segments, a 1-loop segmented ring can be constructed. There is no twist in the 1-loop segmented ring, and each rod segment is subject to uniform bending in the plane of the ring which depends on κ_n and κ_0 . An example of an 8-segment ring (i.e., octagon) with $\kappa_0 = 0$ is shown in Fig. 1 B, ii. This 8-segment ring can also form the 2-loop curved-sided square shown in Fig. 1 B, iii by disconnecting one corner shared by two

Significance

Multistability has emerged as a powerful platform to design functional structures for shape change, property tuning, and multimodal actuation. Most multistable structures are constructed by connecting multiple bistable units. Here, we introduce a concept of segmented rings with intrinsic multistability by programming the natural curvature of the rod segments. Guided by theoretical modeling, simulation, and experimental validation, we demonstrate that a segmented ring with a rectangular cross-section can exhibit up to six distinct planar stable states characterized by uniform bending in each segment. The segmented rings constitute what are probably the simplest elastic structural entities with multiple stable states, and they will serve to expand the application space of functional multistable structures.

Author affiliations: aDepartment of Mechanical Engineering, Stanford University, Stanford, CA 94305; and bSchool of Engineering and Applied Sciences, Harvard University, Cambridge, MA 02138

Author contributions: R.R.Z. designed research; L.L., S.L., J.D., and J.W.H. performed research; L.L., S.L., J.D., J.W.H., and R.R.Z. analyzed data; and L.L., S.L., J.W.H., and R.R.Z. wrote the paper.

The authors declare no competing interest.

This article is a PNAS Direct Submission.

Copyright © 2024 the Author(s). Published by PNAS. This article is distributed under Creative Commons Attribution-NonCommercial-NoDerivatives License 4.0 (CC BY-NC-ND).

¹L.L. and S.L. contributed equally to this work.

²To whom correspondence may be addressed. Email:

This article contains supporting information online at https://www.pnas.org/lookup/suppl/doi:10.1073/pnas. 2405744121/-/DCSupplemental.

Published July 24, 2024

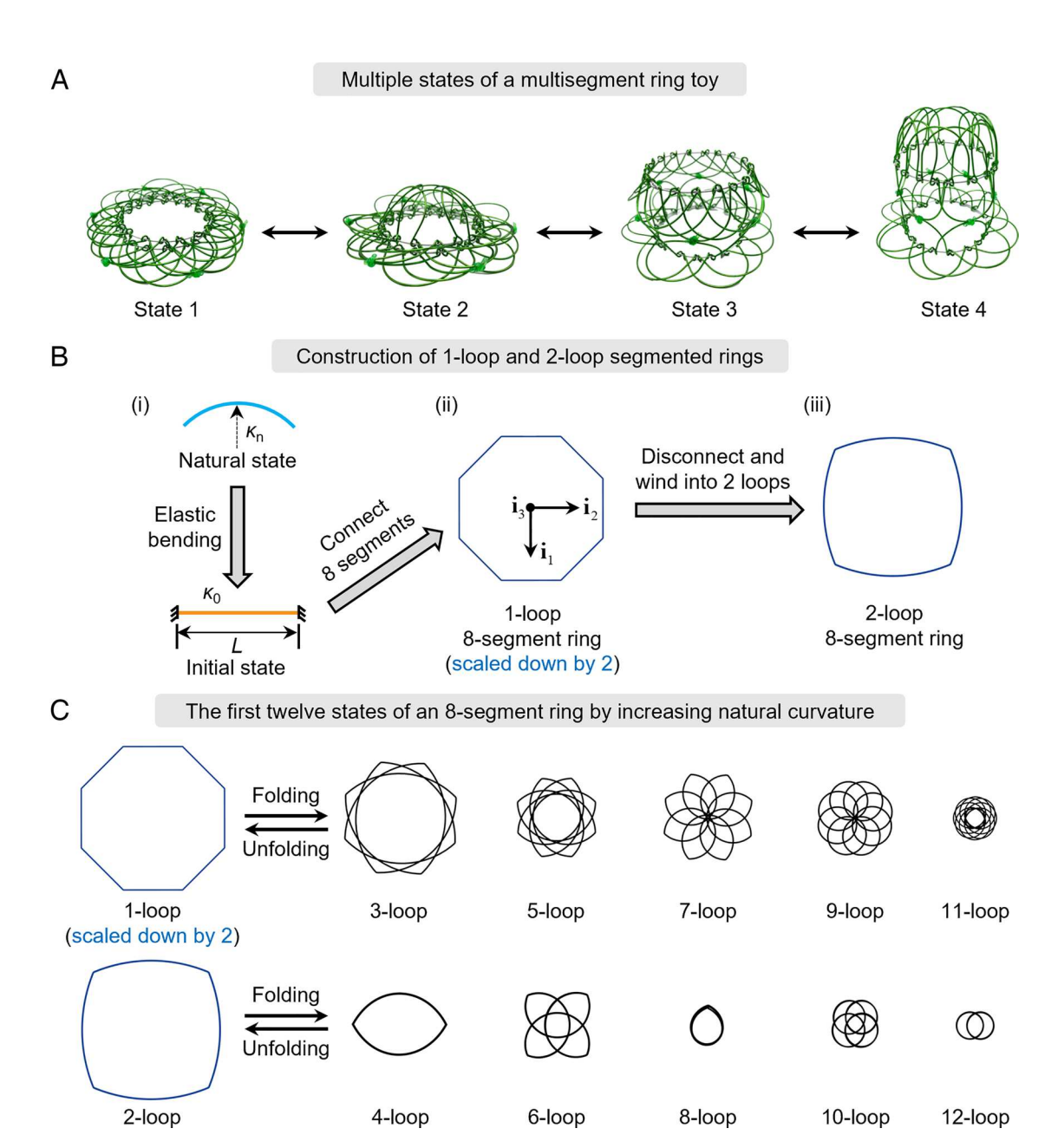


Fig. 1. Multistable segmented rings. (*A*) Multiple states of a multisegment ring toy with tunable height. The toy can transform into different states by selectively controlling the configuration of different layers. (*B*) Construction of 1-loop and 2-loop rings using multiple rod segments. The rod segment of length *L* (blue) has a natural curvature κ_n that can be elastically reconfigured via bending to an initial state (orange) with initial curvature κ_0 (*i*). Note that both κ_n and κ_0 can be either zero or nonzero. Connecting multiple segments end-to-end will result in a planar 1-loop segmented ring (*ii*), such as an 8-segment ring (i.e., octagon) with κ_0 = 0. Disconnecting this 1-loop segmented ring and winding one end by 2π and then reconnecting will result in a 2-loop segmented ring (*iii*), which has a uniform edge radius $R = L_T/2\pi$. (C) The first 12 planar equilibrium states of an 8-segment ring. Each of these states is stable within a specific range of the natural curvature depending on the rod cross-sectional geometry. States with loop numbers larger than 12 are repeating configurations of smaller sizes. The *m*-loop state has a uniform edge radius $R = L_T/[2(m-1)\pi]$ except for the 8-loop state with a nonuniform radius.

adjacent segments, winding one end by 2π , and reconnecting the two ends. The 2-loop ring also has no twist, but one loop crosses over the other. Due to the elastic deformation introduced during the winding process, each rod which was straight in the 1-loop state has an initial radius $R = L_T/2\pi$ in the 2-loop state (with $L_T = 8L$ being the total length of all rod segments). By using this strategy, we can also build 2-loop rings with straight segments that possess predefined natural curvatures (*SI Appendix*, Fig. S1). The segmented rings can transform into other stable states with larger loop numbers under application of external load (e.g., bending or twisting). For example, the 1-loop segmented ring can fold into a 3-loop state, and the 2-loop segmented ring can fold into a 4-loop state, as shown in Fig. 1*C* and Movie S1 for an 8-segment ring.

By increasing the natural curvature of the rod segment, the 1-loop and 2-loop segmented rings can transform into additional stable states spontaneously by structural instability or under external load. Fig. 1C presents the first twelve planar equilibrium states of the 1-loop and 2-loop 8-segment rings. Remarkably, with one exception that will be mentioned later, the rod segments in all states shown in Fig. 1C have a uniform bending moment. For a specific rod cross-section, stability of each of these states can be achieved by adjusting the natural curvature of the rod segments. These states include all the nonrepeating planar configurations of the 8-segment ring with zero or positive natural curvature (the segment with positive natural curvature bends toward the center of the ring). States with loop numbers larger than 12 are smaller-sized repeated configurations (SI Appendix, Fig. S2).

By decreasing the natural curvature of the rod segments such that they bend away from the center of the ring, we can obtain a new group of planar equilibrium states of the 8-segment ring with negative natural curvature (SI Appendix, Fig. S3). The planar equilibrium states of the 8-segment ring with negative natural curvature are inverted configurations of the ring with zero or positive natural curvatures. Additionally, when considering the self-contact between the layers (31), the ring can be stable in some 3D states (SI Appendix, Fig. S4). In this work, we mainly focus on the planar equilibrium states of the segmented ring with nonnegative natural curvatures. The planar states are named by the loop number, which is characterized by the number of loops needed to wind the disconnected 1-loop ring to achieve a specified state. Specifically, to form the *m*-loop state (*m* is an integer), we need to wind one end of the disconnected 1-loop state with additional (*m*–1) loops, or equivalently to wind by $2(m-1)\pi$ (Movie S2). As a result, if the m-loop state has a uniform edge radius, the radius is equal to

$$R = \frac{L_{\mathrm{T}}}{2(m-1)\pi}.$$
 [1]

All the states with a loop number larger than or equal to 3 can be achieved by folding either the 1-loop or the 2-loop configuration of the segmented ring. Additionally, higher loop number states can be mutually stable and transform between one another, depending on the natural curvature, loading method, and cross-sectional geometry. Therefore, as will be illustrated, rational design methods can be employed to construct segmented rings that are stable in multiple

In this paper, we thoroughly investigate the multistability of segmented rings by seeking all possible planar stable states and identifying their corresponding natural curvature ranges. For this purpose, we use a combination of theoretical modeling, finite element analysis (FEA), and experimental validation. In particular, 1-loop and 2-loop rings with different segment numbers are considered (see SI Appendix, Figs. S2 and S5-S10 for the planar equilibrium states of rings with segment numbers n varying from 4 to 10). The natural curvature range within which the segmented rings are stable is predicted by a stability analysis based on requiring positive energy variations about the equilibrium state. The transitions between different stable states of 1-loop and 2-loop segmented rings are studied using FEA and are validated experimentally. To highlight just one finding, it will be shown that 1-loop 8-segment rings can be designed to have up to six planar stable states, three of which are associated with the 1-loop state and three with the 2-loop state. We believe such rings may be the simplest elastic structural systems capable of displaying this level of multistability. In addition, we envision that the strategy of programming natural curvature of segmented rings to guide their multistability could be

which they are stable. The approach is carried out within the framework of Kirchhoff rod theory, which is a generalized version of the basic framework introduced in ref. 27. Compared to the basic framework, which applies only to several specific rings (e.g., circular rings in ref. 27 and curved-sided hexagram that can fold into a 3-loop line in ref. 23), this general framework can be used for the elastic stability analysis of arbitrary planar segmented rings with uniform edge curvature, regardless of the number of segments or layers. As shown in Fig. 1B, consider a *n*-segment ring lying in the $(\mathbf{i}_1, \mathbf{i}_2)$ plane with each segment having length L and a uniform radius of curvature $R = 1/\kappa_0$ about the i_3 -axis in the initial equilibrium state ($\kappa_0 = 0$ for a straight-sided segment). In this state, the principal axis along the thickness direction of the cross-section lies in the $(\mathbf{i}_1, \mathbf{i}_2)$ plane with bending stiffness B_1 about this axis, and the principal axis along the height direction of the crosssection is aligned with the i_3 -axis with bending stiffness B_3 . The torsional stiffness about the rod axis is denoted by B_2 . The curvatures about the respective principal axes are κ_1 , κ_2 , and κ_3 . In the planar equilibrium state, the uniform natural curvature κ_{n} is about the i₃-axis such that the bending moment in each segment of the ring about this axis is $B_3(R^{-1}-\kappa_n)$. Adjacent segments are "welded" at the joints to form the planar configuration. The rod segments are inextensible and unshearable with linear bending and twisting constitutive behavior. Thereby, the strain energy in a rod segment in any state is given by

$$SE = \frac{1}{2} \int_{0}^{L} \left[B_{1} \kappa_{1}^{2} + B_{2} \kappa_{2}^{2} + B_{3} (\kappa_{3} - \kappa_{n})^{2} \right] ds,$$
 [2]

where κ_1 , κ_2 vanish in the initial state and s is the arc length

The rings lose stability via deformations that involve out-of-plane deflections and twists that are described using Euler angles to measure changes from the initial state. The curvature components can be expressed in terms of the Kirchhoff theory Euler angles (α, β, γ) as in ref. 27

$$\begin{split} \kappa_1 &= \frac{d\beta}{ds} - \frac{\omega}{R} + O_3, \\ \kappa_2 &= \frac{d\omega}{ds} + \frac{\beta}{R} + O_3, \\ \kappa_3 &= \frac{1}{R} \left(1 - \frac{\omega^2}{2} - \frac{\beta^2}{2} \right) - \beta \frac{d\omega}{ds} + \frac{d(\alpha\beta)}{ds} + O_4, \end{split}$$
 [3]

with $\omega = \alpha + \gamma$, and the definition of the Euler angles is shown in SI Appendix, Fig. S11. Here, O_3 and O_4 represent the terms of order cubic and quartic, respectively, which can be neglected in evaluating the energy change to order O_2 . This energy change for a n-segment ring is

$$P_{2} = \frac{1}{2} \sum_{i=1}^{n} \int_{0}^{L} \left\{ B_{1} \left(\frac{d\beta^{(i)}}{ds} - \frac{\omega^{(i)}}{R} \right)^{2} + B_{2} \left(\frac{d\omega^{(i)}}{ds} + \frac{\beta^{(i)}}{R} \right)^{2} - B_{3} M \left[\left(\frac{\beta^{(i)}}{R} \right)^{2} + \left(\frac{\omega^{(i)}}{R} \right)^{2} + \frac{2\beta^{(i)}}{R} \frac{d\omega^{(i)}}{ds} - \frac{2}{R} \frac{d(\alpha^{(i)}\beta^{(i)})}{ds} \right] \right\} ds.$$
[4]

used for the design of other multifunctional, reconfigurable, and deployable structures.

Elastic Stability Analysis of Segmented Rings

We begin by briefly outlining the elastic stability analysis of segmented rings to determine the natural curvature range within

Here, the superscript *i* denotes the quantity associated with the *i*-th segment, and $M = 1 - R\kappa_n$ is a dimensionless parameter measuring the bending moment introduced by the natural curvature in the initial state. The condition required for the state in question to be stable is that $P_2 > 0$ for all nonzero admissible displacements, excluding rigid body motions, and this generates the stability eigenvalue problem. Obviously, when $R\kappa_n = 1$, i.e., M = 0, P_2 satisfies the condition because $d\beta^{(i)}/ds-\omega^{(i)}/R$ and $d\omega^{(i)}/ds+\beta^{(i)}/R$ vanish for rigid body motions, meaning that the segmented ring is always stable when its natural curvature $\kappa_n=1/R$. In the stability analysis, we determine the natural curvature range, $R\kappa_n^- < R\kappa_n < R\kappa_n^+$, such that the stability condition is satisfied, where $R\kappa_n^-$ is the largest eigenvalue smaller than 1 and $R\kappa_n^+$ the smallest eigenvalue larger than 1 for which P_2 is stationary with respect to all admissible displacements.

The details on finding the stability limits for κ_n are provided in *SI Appendix*, section S1. In particular, the last term in Eq. 4 involving $\alpha^{(i)}\beta^{(i)}$ can be replaced by terms involving $\omega^{(i)}$ and $\beta^{(i)}$ by making use of conditions at the segment corners (*SI Appendix*, Eq. S18). The final form of the stability functional is expressed in terms of the out-of-plane displacement and the twist, and the geometric constraints that must be satisfied at the corners joining the segments are specified (*SI Appendix*, Eq. S30). For 1-loop rings formed by straight rod segments, 1/R = 0 in Eq. 3, and their stability ranges can be determined following the same solution process (*SI Appendix*, section S2).

1-Loop Segmented Rings

Next, we introduce the multiple transition states of 1-loop segmented rings with nonnegative natural curvatures, as shown in Fig. 2. When the loop number is an integer multiple of the segment number, i.e., m = kn ($k = 1, 2, \cdots$), the state has a nonuniform radius. All these states have the same total length L_T and can be stable when their natural curvatures are within a specific range (see *SI Appendix*, Table S1 for stability limits of the dimensionless natural curvature $\kappa_n L_T/2\pi$ of the states with cross-sectional height-to-thickness ratio h/t = 4 and Poisson's ratio $\nu = 0.3$), which are determined using the method introduced in *Elastic Stability Analysis of Segmented Rings* (Verification of this method using FEA

is presented in SI Appendix, Fig. S13 and section S3). These states are first found by examining the transition behavior of the 1-loop segmented rings with different natural curvatures through FEA. They are then validated experimentally (*SI Appendix*, Fig. S12). Details on FEA and the experiments are provided in Materials and Methods, and details on how to find all achievable planar stable states of 1-loop segmented rings are presented in SI Appendix, Fig. S14 and section S4. Here, seven types of 1-loop rings with segment numbers ranging from 2 to 8 are studied, which are referred to as birod, triangle, square, pentagon, hexagon, heptagon, and octagon, respectively (Fig. 2A). Dimensionless natural curvature ranges for the stability and the dimensionless strain energy (UL_T/B_3) at the stability limits of these 1-loop segmented rings are shown in Fig. 3 A and B, which are dependent on the cross-sectional geometry. Note that the strain energy at the stability limits of a segmented ring is given by $U = B_3 L_T (R^{-1} - \kappa_n)^2 / 2$. The stability range of the natural curvature gradually widens as h/t increases. At the upper stability limit, the triangle (n = 3) has the highest natural curvature and strain energy among various 1-loop segmented rings, followed by the birod. As a result, the triangle can store the most strain energy without losing stability at the upper limit (Fig. 3B), surpassing even that of the 1-loop circular ring with the same total length. By contrast, the square (n = 4) has the lowest natural curvature and strain energy at the upper limit. At the lower stability limit (represented by dashed lines in Fig. 3 A and B), the magnitude of the natural curvature and strain energy of 1-loop segmented rings monotonically increases with the segment number. It is interesting that the 1-loop segmented rings can store much more strain energy at the lower stability limit than at the upper stability limit. Moreover, as the segment number *n* increases, the strain energy at the stability limits gradually converges to that of a 1-loop circular ring (with the same

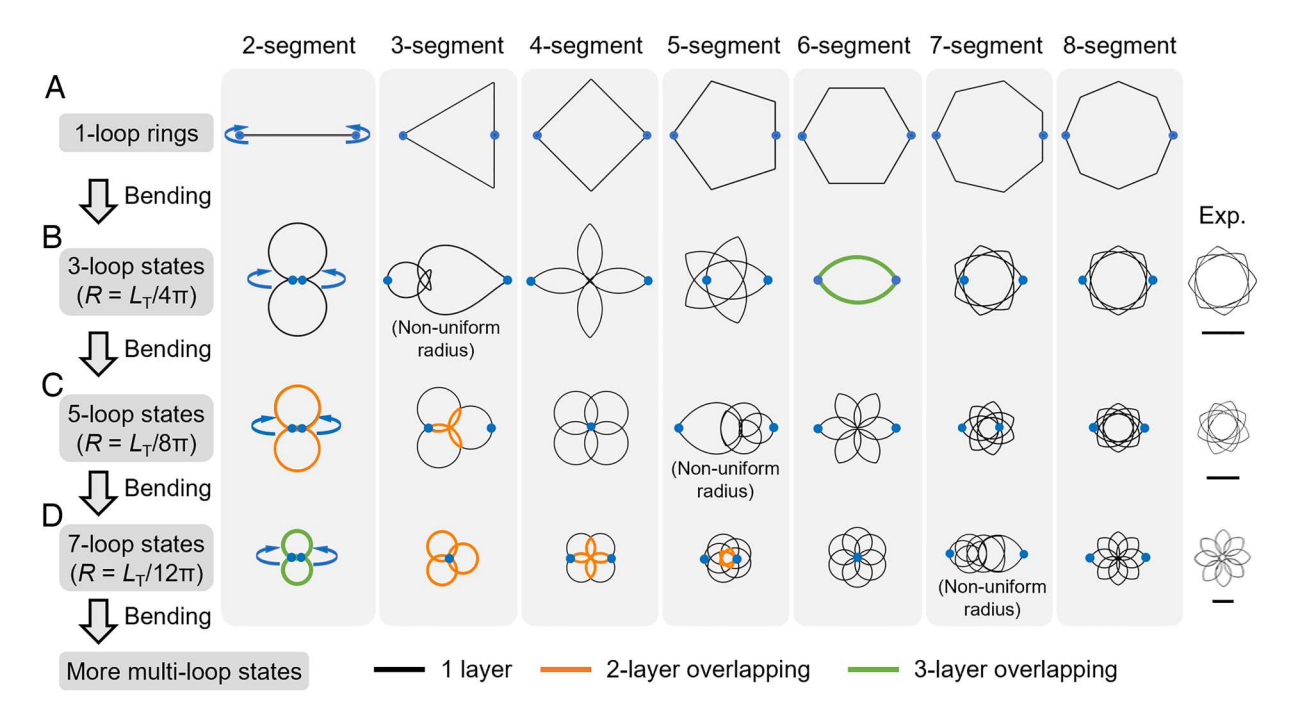
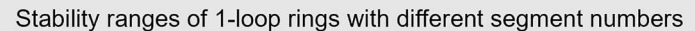


Fig. 2. Transition states of 1-loop segmented rings with nonnegative natural curvatures. All these states can be stable within specific natural curvature ranges, which are provided in *SI Appendix*, Table S1 for the case of rectangular cross-sections with h/t = 4 and Poisson's ratio $\nu = 0.3$. (*A*) The 1-loop segmented rings are regular polygons when the segment number is larger than 2. The 1-loop 2-segment ring is composed of two straight rods welded at both ends and is referred to as a birod. (*B*) By applying a pair of bending loads at the loading points (blue dots), the 1-loop segmented rings can transform into the 3-loop states with uniform edge radii $R = L_T/4\pi$ (except for the 3-segment ring). (*C*) The 3-loop states transform into the 5-loop states with uniform edge radii $R = L_T/8\pi$ (except for the 5-segment ring). (*D*) The 5-loop states can transform into 7-loop states with uniform edge radii $R = L_T/12\pi$ (except for the 7-segment ring). By increasing the natural curvature of the rod segments, additional stable transition states with higher loop numbers can be achieved under external bending loads. Experimental validation for the 1-loop 8-segment ring is shown in the rightmost column. (Scale bars: 10 cm.) Experimental images of all these states are presented in *SI Appendix*, Fig. S12.



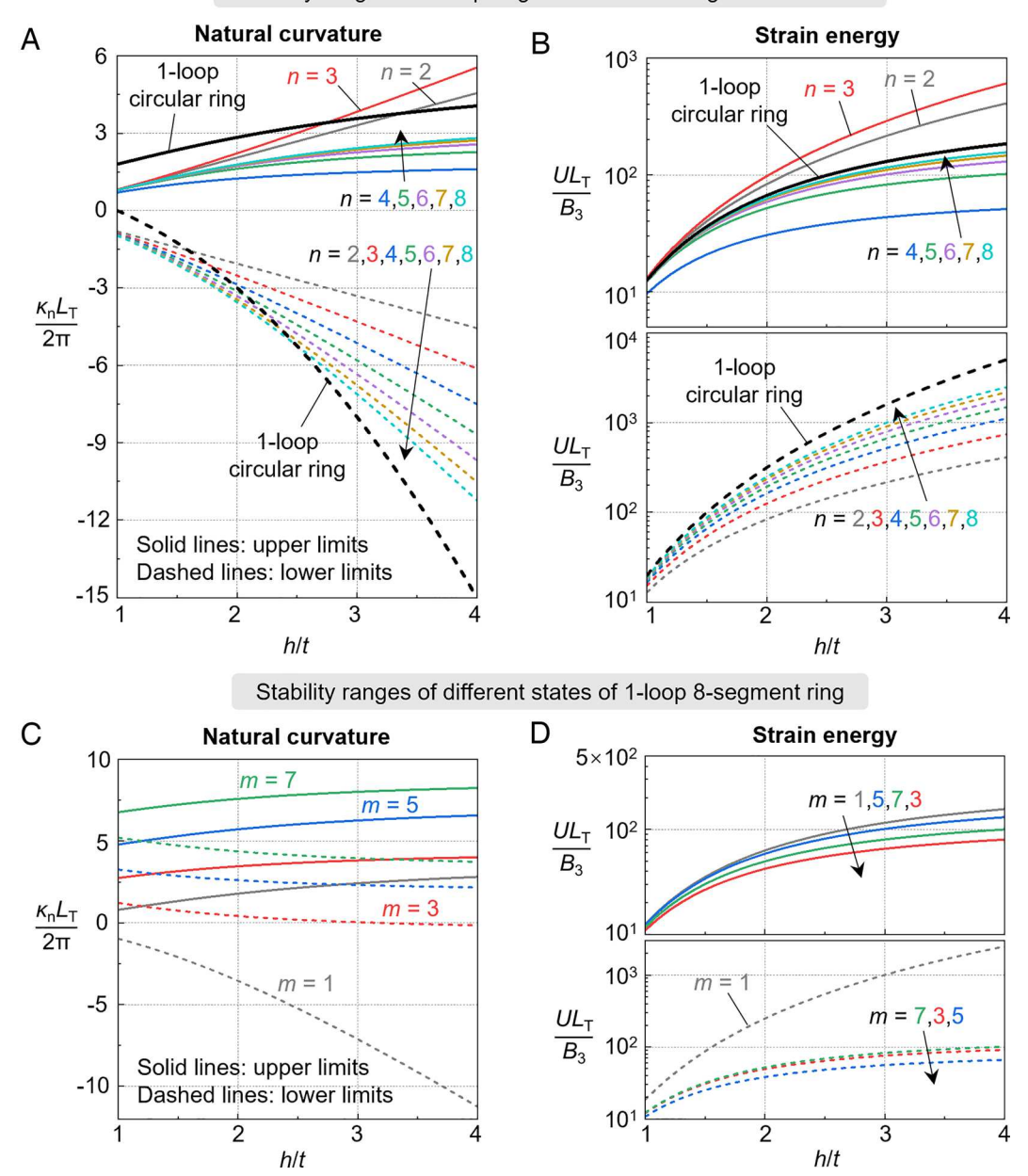


Fig. 3. Stability ranges of 1-loop segmented rings having rectangular cross-section with height-to-thickness ratio h/t and ν = 0.3. (A) Stability limits for the dimensionless natural curvature $\kappa_n L_T/2\pi$ of 1-loop rings (i.e., birod and polygons) with different segment numbers n. (B) Dimensionless strain energy UL_T/B_3 at the stability limits of 1-loop rings with different segment numbers n. (C) Stability limits for the dimensionless natural curvature $\kappa_n L_1/2\pi$ of the m-loop state of 1-loop 8-segment ring. (D) Dimensionless strain energy UL_T/B_3 at the stability limits of the m-loop state of 1-loop 8-segment ring.

total length). The natural curvature at the stability limits converges to that of a 1-loop circular ring minus one due to the difference between their initial edge curvatures: The initial edge curvature of the 1-loop circular ring is 1/R while that of the 1-loop segmented ring is zero. In particular, the natural curvature range for the stability of a 1-loop circular ring can be analytically solved (SI Appendix, section S5), which is given by

$$1 - b_1 < \frac{\kappa_n L_T}{2\pi} < \frac{2 - b_1 - b_2 + \sqrt{b_1^2 + 14b_1b_2 + b_2^2}}{2}. \quad [5]$$

Here, $b_1 = B_1/B_3 = (h/t)^2$ and $b_2 = B_2/B_3 = 2[1 - (192/\pi^5)(t/h)]$ $\tanh(\pi h/2t)]/(1+\nu)$ are the dimensionless out-of-plane bending and torsional stiffnesses of a rod with rectangular cross-section and ν is the Poisson's ratio. Note that the analytical solution for

the stability range of the 1-loop circular ring was first obtained by Manning and Hoffman in ref. 29, although it was denoted by different symbols.

By applying a pair of bending loads (blue arrows) at the two loading points (blue dots), the stable 1-loop segmented rings (with nonnegative natural curvatures) transform into various 3loop states with curved edges, as shown in Fig. 2B and Movie S3. Note that the transitions between these stable configurations are path independent. For the ease of applying bending, the loading points on the 1-loop state are at a pair of opposite corners for rings with even segment numbers, and are at one corner and the middle point of its opposite edge for rings with odd segment numbers. The transition of 1-loop segmented rings to 3-loop and higher odd-numbered loop states, all of which are untwisted, but not to even-numbered loops, is the topological counterpart of

the behavior of 1-loop circular rings which transition to higher odd-numbered circular loops (28, 29). Except for the 3-segment ring, all of the 3-loop states have the same edge radius $R = L_T/4\pi$. In particular, the 3-loop state of the 2-segment ring is an "8" shape consisting of two circles, and the 3-loop state of the 6-segment ring is a 3-layer fully overlapping peach core shape (denoted by green). The natural curvature ranges for the stability and the corresponding strain energy at the stability limits of 3-loop states with different segment numbers are provided in SI Appendix, Fig. S15. Results show that in the 3-loop states, the 7-segment ring has the highest natural curvature and strain energy, and the 8-segment ring has the lowest natural curvature and strain energy at the upper stability limit. Moreover, the 3-loop states of the 2-segment, 3-segment, and 6-segment rings have the same upper limit for the natural curvature and strain energy. At the lower stability limit, the 5-segment and 4-segment rings can store the most and least strain energy, respectively. Additionally, with the increasing segment number, the strain energy at the stability limits of 3-loop segmented rings approaches that of the 3-loop circular ring (with the same total length), and the natural curvature at the stability limits approaches that of the 3-loop circular ring minus one. The stability range of a 3-loop circular ring also has an analytical solution. In SI Appendix, section S6, we derived the stability limits for the natural curvature of an *m*-loop circular ring $(m \ge 2)$, as

8-segment ring are shown in the rightmost part of Fig. 2, demonstrating a good agreement with FEA results. Experimental images for all other states are presented in *SI Appendix*, Fig. S12, and transition processes between different states from FEA are shown in Movie S3. It is worth noting that additional planar transition states with higher loop numbers are also possible by further increasing the natural curvature of the rod segments (see *SI Appendix*, Figs. S2 and S5–S8 for more planar equilibrium states of segmented rings with the segment number varying from 4 to 8). For 2-segment and 3-segment rings, the higher loop number states have the same configurations as their 3-loop and 5-loop states, respectively.

The different transition states of 1-loop segmented rings can be mutually stable when their natural curvature ranges for stability overlap. The natural curvature ranges for mutually stable states of 1-loop rings with different segment numbers are presented in SI Appendix, Table S2 for the case of h/t = 4 and $\nu = 0.3$. It is shown that, apart from the 2-segment and 3-segment rings, the other 1-loop segmented rings can only be mutually stable in at most three neighboring transition states. To better illustrate this, Fig. 3C plots the natural curvature ranges for the stability of different transition states of the 8-segment ring with h/t varying from 1 to 4. One can see that the natural curvatures at the stability limits increase with the loop number m. For two neighboring transition states, they can be mutually stable in a wide natural curvature range. For example, the 1-loop and 3-loop states are mutually stable in the range between

$$\frac{\kappa_{\rm n}^{\pm}L_{\rm T}}{2\pi} = \frac{1}{2} \left[m(2 - b_1 - b_2) + \sqrt{m^2 b_1^2 + (2m^2 \pm 8m + 4)b_1b_2 + m^2 b_2^2} \right].$$
 [6]

Note that the plus-minus sign is minus at the lower stability limit and plus at the upper stability limit. The stable 3-loop states can transition to the 5-loop states and the stable 5-loop states can transition to the 7-loop states under external bending loads, as shown in Fig. 2 C and D and Movie S3. Apart from the 5-loop 5-segment ring and the 7-loop 7-segment ring, all other 5-loop and 7-loop states have uniform edge radii of $L_{\rm T}/8\pi$ and $L_{\rm T}/12\pi$, respectively. The natural curvature ranges for the stability and the strain energy at the stability limits of the 5-loop and 7-loop states with different segment numbers are presented in SI Appendix, Figs. S16 and S17. Similarly, the strain energy of the 5-loop and 7-loop states at the stability limits tends to converge to those of 5-loop and 7-loop circular rings with the same total lengths, and their natural curvature limits approach those of 5-loop and 7-loop circular rings minus one.

As an example, the transition behavior of a 1-loop 8-segment ring with different natural curvatures under external bending loads is further examined by FEA in SI Appendix, Fig. S18 and section S7, where the moment and energy curves during transition and the transition processes are presented. It is shown that for an initially stable 1-loop 8-segment ring, when the natural curvature is smaller than zero, it transitions to the inverted 1-loop state under external bending loads (other inverted states in *SI Appendix*, Fig. S3 are possible by further decreasing the natural curvature). When the natural curvature is between zero and the upper stability limit ($\kappa_n L_T / 2\pi = 2.81$), the 1-loop 8-segment ring transitions to the 3-loop state. However, when the natural curvature exceeds the upper stability limit, the 1-loop ring is no longer stable. In this case, the ring first snaps to one stable state and then transitions to another state under external bending loads. Experimental images of the transition states (3-loop, 5-loop, and 7-loop) of the 1-loop

the gray solid line and the red dashed line when h/t > 1.2. However, three neighboring transition states can only be mutually stable in a relatively narrow range, such as the range between the gray solid line and the blue dashed line when h/t > 3 within which the 1-loop, 3-loop, and 5-loop states are mutually stable. Strain energy at the stability limits of the different states of the 8-segment ring is compared in Fig. 3D. It is evident that the 8-segment ring can store the most strain energy in its 1-loop state. Particularly, at the lower stability limit, the strain energy of the 1-loop state is one order of magnitude larger than that of other states when h/t > 3.

2-Loop Segmented Rings

As noted in Fig. 1, 1-loop segmented rings can be wound to form 2-loop segmented rings (the experimental winding process is shown in Movie S1). In this section, we will demonstrate that the 2-loop segmented rings can transition into a series of evennumbered, untwisted, multiloop states under external loads. Now, odd-numbered loop states without twist are topologically excluded. In analogy to the 1-loop case, we obtain these states (Fig. 4) by studying the transition behavior of the 2-loop segmented rings with different nonnegative natural curvatures using FEA. Also, these new states have nonuniform radii when the loop number is an integer multiple of the segment number, i.e., m = kn ($k = 1, 2, \cdots$). The stable states are validated through experiments (*SI Appendix*, Fig. S19). For the 2-loop segmented rings, we consider the segment numbers varying from 4 to 10, and they have the same total length as the 1-loop rings. Stability limits for the dimensionless natural curvature $\kappa_n L_T/2\pi$ of these 2-loop segmented rings and their transition states are provided in SI Appendix, Table S3 for the case of h/t = 4 and $\nu = 0.3$. As shown in Fig. 4A, with odd

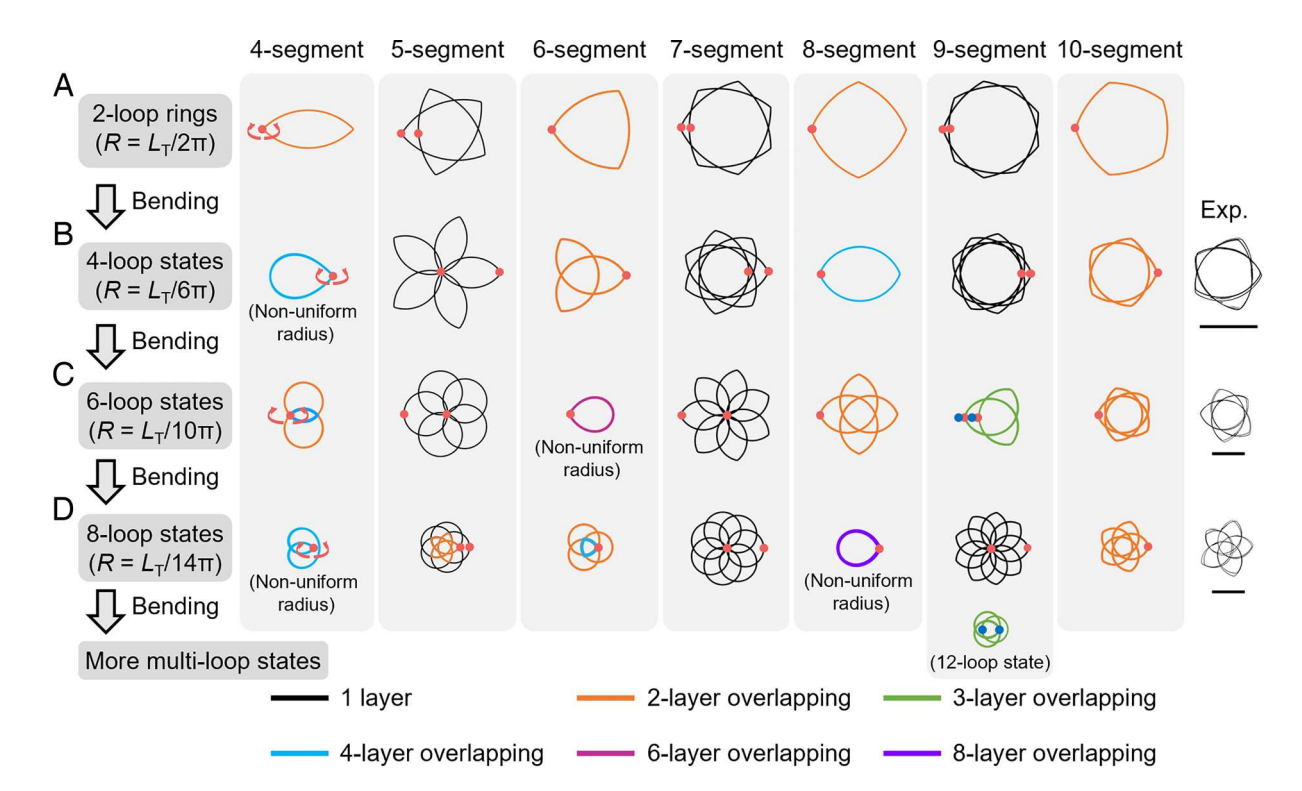
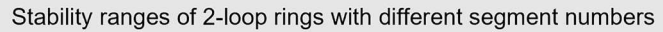


Fig. 4. Transition states of 2-loop segmented rings with nonnegative natural curvatures. The natural curvature ranges for the stability of these states are provided in SI Appendix, Table S3 for the case of h/t = 4 and $\nu = 0.3$. (A) The 2-loop segmented rings have a uniform edge radius $R = L_T/2\pi$. (B) By applying a pair of bending loads at the loading points (red dots), the 2-loop segmented rings can transform into the 4-loop states with a uniform edge radius $R = L_T/6\pi$ (except for the 4-segment ring). (C) The 4-loop states can transform into the 6-loop states with a uniform radius $R = L_T/10\pi$ (except for the 6-segment ring). (D) The 6-loop states can transform into the 8-loop states with a uniform edge radius $R = L_T/14\pi$ (except for the 8-segment ring). By increasing the natural curvature of the rod segments, additional stable transition states with higher loop numbers can be achieved. Experimental validation for the 2-loop 10-segment ring is shown off to the Right. (Scale bars: 10 cm.) Experimental images of all these states are presented in SI Appendix, Fig. S19.

segment numbers (n = 5, 7, 9), the edges of the 2-loop rings cross each other, forming the shapes of curved-sided pentagram, heptagram, and nonagram, respectively. With even segment numbers (n = 4, 6, 8, 10), the 2-loop rings are 2-layer overlapping (denoted by orange), and are presented as peach core shape, curved-sided triangle, curved-sided square, and curved-sided pentagon, respectively. All these 2-loop segmented rings have the same edge radius $R = L_T/2\pi$ in the initial state and their stability ranges for the natural curvature and the strain energy at the stability limits as a function of *hlt* are plotted in Fig. 5 *A* and *B*. It is seen that at the upper stability limit, the curved-sided pentagram (n = 5) has the highest natural curvature and strain energy, and the 2-layer overlapping curved-sided triangle (n = 6) has the lowest natural curvature and strain energy among various 2-loop segmented rings. In particular, the strain energy at the upper limit of the curvedsided pentagram is even higher than that of a 2-loop circular ring (with the same total length), indicating that it can store more strain energy than the 2-loop circular ring. At the lower stability limit, the 2-layer overlapping peach core (n = 4) has the highest natural curvature and strain energy. As in the case of the 1-loop rings, when the segment number increases, the strain energy of 2-loop segmented rings at the stability limits converges to that of the 2-loop circular ring, and the natural curvature at the stability limits approaches that of the 2-loop circular ring minus one. Note that the natural curvature at the stability limits of a 2-loop circular ring can be obtained using Eq. 6 with m = 2.

When subjected to a pair of bending loads at the location of the red dots (for the 2-layer overlapping state, the bending loads are applied at the same position but in different layers), stable 2-loop segmented rings transform into their 4-loop states (Fig. 4B and Movie S4). Apart from the 4-loop state of the 4-segment ring, all other 4-loop states share a uniform edge radius $R = L_T/6\pi$. In particular, the 4-loop states of the 6-segment and 10-segment rings are 2-layer overlapping (denoted by orange), and that of the 8-segment ring is 4-layer overlapping (denoted by blue). The stability limits for the natural curvature and the corresponding strain energy of 4-loop states with different segment numbers are presented in SI Appendix, Fig. S20, which indicates that the 9-segment ring has the highest natural curvature and strain energy at the upper stability limit and the 7-segment ring has the highest natural curvature and strain energy at the lower stability limit among various 2-loop segmented rings. As expected, in the 4-loop states, the strain energy at the stability limits converges to that of the 4-loop circular ring, and the natural curvature at the stability limits converges to that of the 4-loop circular ring minus one. By applying a pair of bending loads at the loading points (red dots), stable 4-loop states can transform into 6-loop states and stable 6-loop states can transform into 8-loop states, as shown in Fig. 4 C and D and Movie S4. Except for the 6-layer overlapping state of the 6-segment ring and the 8-layer overlapping state of the 8-segment ring, all other 6-loop and 8-loop states have uniform edge radii, which are $L_{\rm T}/10\pi$ and $L_{\rm T}/14\pi$, respectively. The natural curvature range for the stability and the corresponding strain energy at the stability limits of various 6-loop and 8-loop states are provided in SI Appendix, Figs. S21 and S22, respectively. Again, the strain energy of these states at the stability limits converges to the circular ring with the same loop number and total length, and the natural curvature approaches that of the circular ring minus one.

To demonstrate the effect of natural curvature on the transition behavior of 2-loop segmented rings, we take the 2-loop 8-segment ring as an example and study its moment and energy variations during transition using FEA (SI Appendix, Fig. S23 and section S8). It is shown that when the natural curvature is within the stability



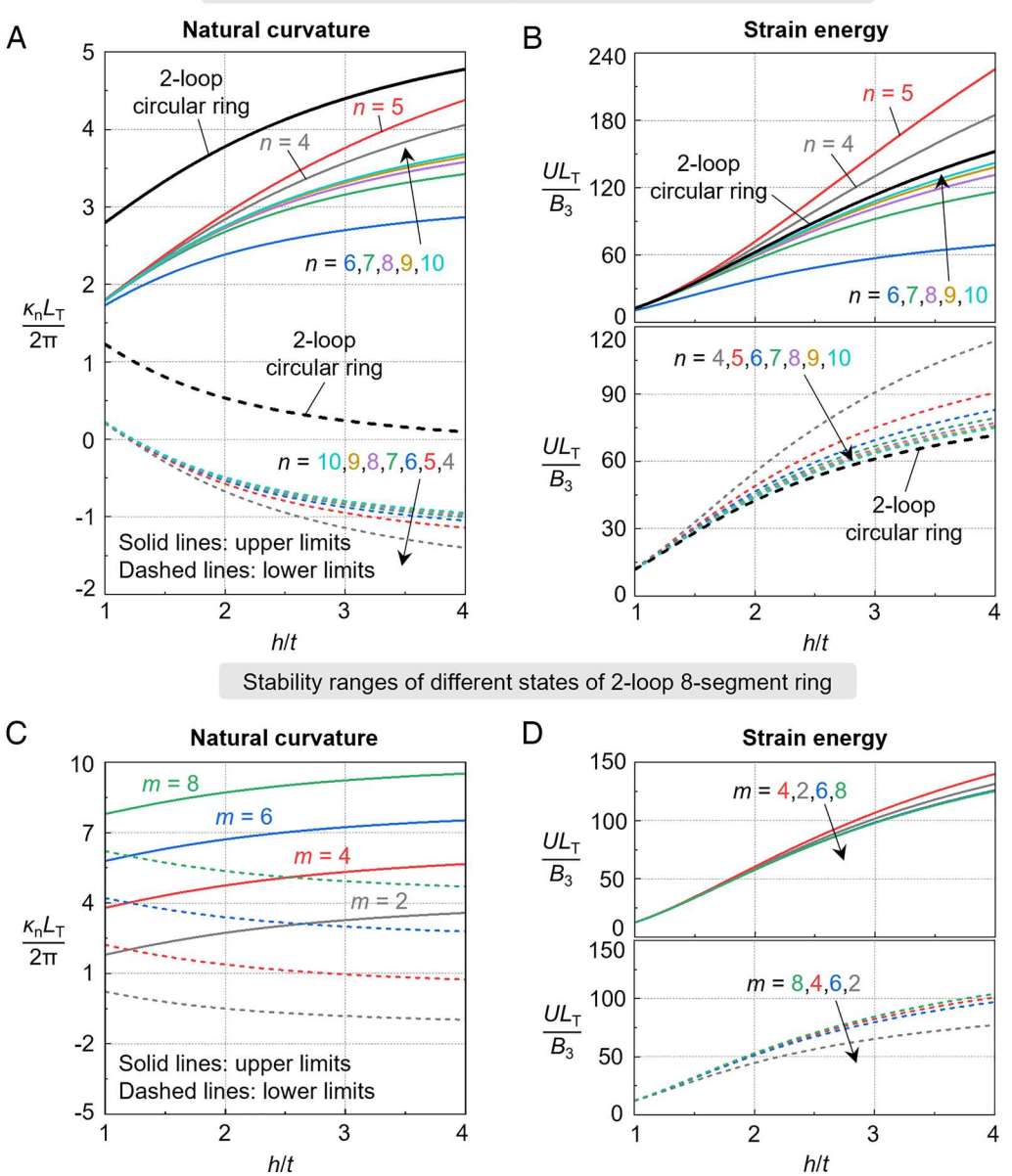


Fig. 5. Stability ranges of 2-loop segmented rings having rectangular cross-section with height-to-thickness ratio h/t and $\nu=0.3$. (A) Stability limits for the dimensionless natural curvature $\kappa_n L_T/2\pi$ of 2-loop rings with different segment numbers n. (B) Dimensionless strain energy UL_T/B_3 at the stability limits of 2-loop rings with different segment numbers n. (C) Stability limits for the dimensionless natural curvature $\kappa_n L_T/2\pi$ of the m-loop state of the 2-loop 8-segment ring. (D) Dimensionless strain energy UL_T/B_3 at the stability limits of the m-loop state of the 2-loop 8-segment ring.

range (but still larger than zero), by applying a pair of bending loads, the 2-loop 8-segment ring folds into the 4-loop state. Otherwise, it first snaps to a stable state and then transitions to another state under external bending loads. Experimental demonstrations for the 4-loop, 6-loop, and 8-loop states of the 10-segment ring are provided in the rightmost part of Fig. 4, which agree with the FEA results very well. Experimental images of all other states are presented in SI Appendix, Fig. S19, and transition processes between different states from FEA are provided in Movie S4. Note that if the natural curvature of the rod segment is further increased, the 2-loop segmented rings could achieve additional planar transition states with higher loop numbers. In SI Appendix, Figs. S2 and S5–S10, we summarized the planar equilibrium states of segmented rings with segment numbers *n* varying from 4 to 10. It is shown that for an n-segment ring, its first n planar equilibrium states have different configurations with corners pointing outward. Starting from the (n+1)-loop state, the ring shows periodic planar configurations with corners pointing inward, and the periodicity of the repeating configurations is *n*. Additionally, the rotational symmetry of these states also exhibits periodicity with a period of n. In one period, the ring can have a planar state with the rotational symmetry corresponding to each divisor of its segment number. For example, the 6-segment ring has 1-fold, 2-fold, 3-fold, and 6-fold rotational symmetry in its 6-loop, 3-loop, 2-loop, and 1-loop states, respectively. Rotational symmetry of the first ten planar equilibrium states of various segmented rings is summarized in SI Appendix, Table S4. More interestingly, for 2-layer and 3-layer overlapping rings, loadings applied to different numbers of layers of the same ring would lead to different configurations. Take the 6-loop state of the 9-segment ring as an example. When bending is applied to a single layer, i.e., one bending load is applied to the bottom layer and the other bending load is applied to the top layer (loading points denoted by the red dots), the 6-loop 9-segment ring transitions to the 8-loop state. When

the bending loads are applied to all layers (loading points denoted by blue dots), however, the 6-loop 9-segment ring folds into a 12-loop state (*SI Appendix*, Fig. S24).

Like the 1-loop segmented rings, the 2-loop segmented rings can be stable in two or three neighboring transition states simultaneously, and the natural curvature ranges for the mutual stability of 2-loop segmented rings with h/t = 4 and $\nu = 0.3$ are provided in *SI Appendix*, Table S5. As an example, Fig. 5*C* plots the natural curvatures at the stability limits of different transition states of the 8-segment ring with respect to h/t. As can be seen, the mutual stability ranges between two neighboring transition states (e.g., 2-loop and 4-loop states) are wide, while the mutual stability ranges between three neighboring transition states (e.g., 4-loop, 6-loop, and 8-loop states) are relatively narrow. Strain energy at the stability limits of the 8-segment rod in different states are shown in Fig. 5D. Results indicate that the 4-loop state has the highest strain energy at the upper stability limit, and the 2-loop state has the lowest strain energy at the lower stability limit. In other multiloop states, there is no significant difference in the strain energy.

Multistable Segmented Rings

Having explored the various stable states of 1-loop and 2-loop segmented rings, we next present an approach to rationally choose the natural curvature to achieve multiple stable states for segmented rings, with the 8-segment ring of h/t = 4 and $\nu = 0.3$ as an example. The stability ranges of dimensionless natural curvature $\kappa_n L_T/2\pi$ for the first twelve states of the 8-segment ring are shown in Fig. 6A. These twelve states comprise all the nonrepeating stable planar configurations of the 8-segment ring with nonnegative natural curvatures (SI Appendix, Fig. S2). States with loop numbers larger than 12 are smaller-sized repeated configurations. Note that the 1-loop to 3-loop states can also be stable when the natural curvature is negative, but we only present the stability regions with nonnegative natural curvatures here. Moreover, the stability regions with dimensionless natural curvature larger than 10 include stable states from the 13-loop to 16-loop states (see SI Appendix, Table S6 for their stability ranges). It is seen that the 8-segment ring can have up to six stable

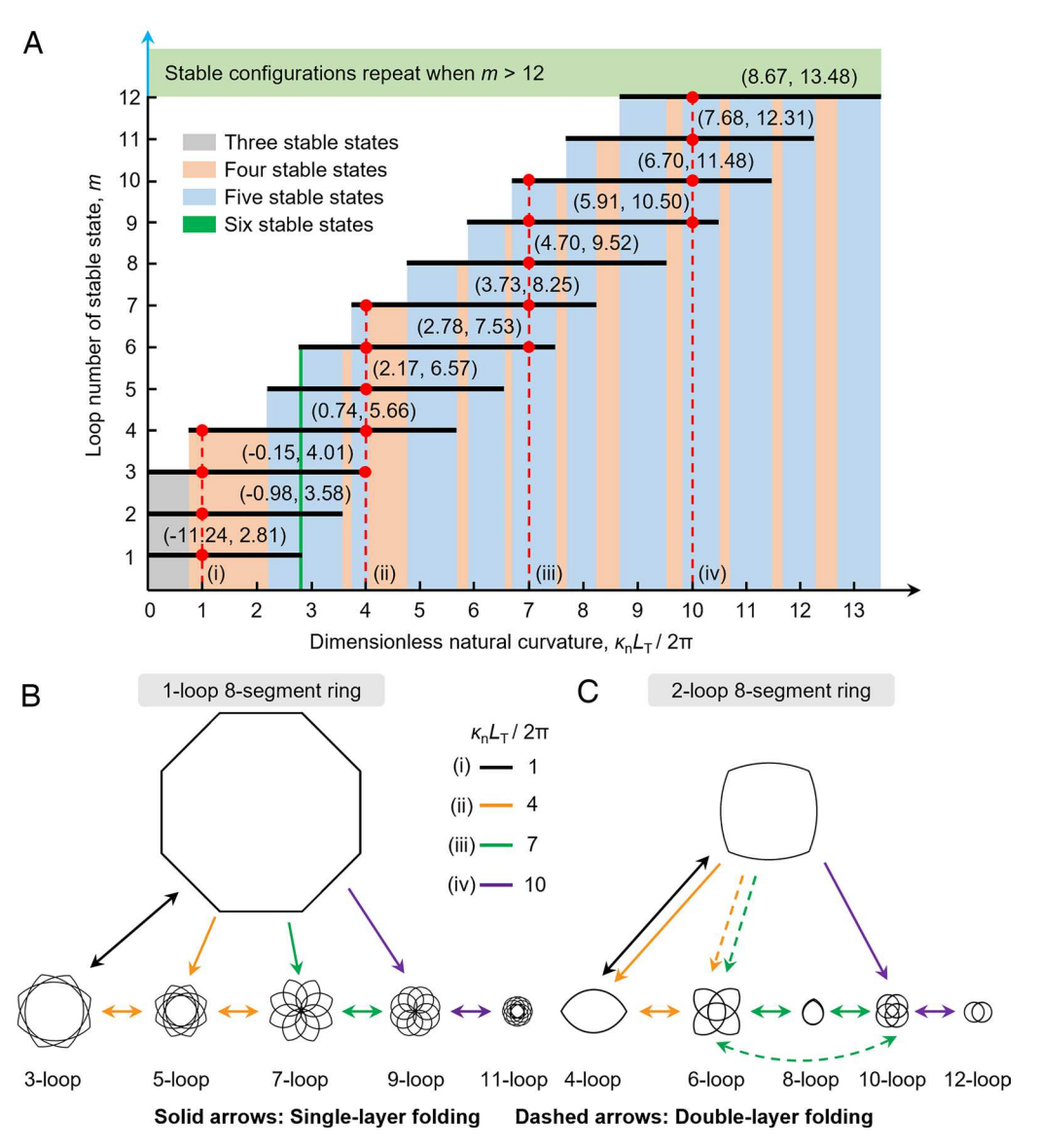


Fig. 6. Phase diagram for the multistability and transitions of 8-segment rings with h/t = 4 and $\nu = 0.3$. (A) Stability ranges of dimensionless natural curvature $\kappa_0 L_7/2\pi$ for the first twelve stable states of 8-segment rings. States with loop numbers larger than 12 are smaller-sized repeated configurations (SI Appendix, Fig. S2). The stability regions with $\kappa_n L_T/2\pi > 10$ include stable states from the 13-loop, 14-loop, 15-loop, and 16-loop states. The red dots denote the stable states corresponding to $\kappa_n L_{\gamma} / 2\pi = 1, 4, 7$, and 10. The numbers in parentheses are the stability range of each state. (B) Transitions between the odd-numbered loop states of 1-loop 8-segment rings with $\kappa_n L_T/2\pi = 1, 4, 7$, and 10. (C) Transitions between the even-numbered loop states of 2-loop 8-segment rings with $\kappa_n L_T/2\pi = 1, 4, 7,$ and 10. The solid arrows denote single-layer folding while the dashed arrows denote double-layer folding. Unidirectional arrows indicate that the initial state is unstable.

states (green region) within a narrow natural curvature range of (2.78, 2.81), three of which are associated with the 1-loop state (1-loop, 3-loop, and 5-loop states) and three with the 2-loop state (2-loop, 4-loop, and 6-loop states). There are twelve different natural curvature ranges for the 8-segment ring to have five stable states (light blue regions), and these ranges cover various combinations of stable states. Further, the 8-segment ring exhibits four stable states (light red regions) in eleven different natural curvature ranges and has three stable states (gray region) when its natural curvature is near zero, i.e., (0, 0.74), within which the 1-loop, 2-loop, and 3-loop states are stable. Based on the stability phase diagram, one can easily determine the corresponding stable states of a segmented ring for a given natural curvature or design a segmented ring to achieve the desired stable states by rationally selecting the natural curvature.

Finally, we show how to achieve the transitions between different states of multistable 8-segment rings. Here, we consider four representative dimensionless natural curvatures, i.e., $\kappa_n L_T / 2\pi = 1$, 4, 7, and 10. The corresponding stable states of these four selected natural curvatures are denoted by red dots in Fig. 6A, which cover all the 12 nonrepeating stable configurations of 8-segment rings with nonnegative natural curvatures. The achievable transition paths between states are grouped with respect to their basic state, i.e., the 1-loop state for rings with odd loop numbers (Fig. 6B) and the 2-loop state for rings with even loop numbers (Fig. 6C). Note that transitions between the states within either of these groups can be achieved by directly applying a pair of bending loads. Unidirectional arrows denote a transition from an initially unstable state to a stable folded state while bidirectional arrows denote a transition between two stable states. Solid arrows indicate that the state transition occurs by single-layer folding, in which bending loads are applied to two different single-layers, while dashed arrows indicate double-layer folding (bending loads are applied to all layers).

For $\kappa_n L_T / 2\pi = 1$ (case-i), the 8-segment ring is stable in the 1-loop to 4-loop states. From Figs. 2 and 4, transitions between the 1-loop and 3-loop states, and the 2-loop and 4-loop states can be achieved by single-layer folding. For $\kappa_n L_T / 2\pi = 4$ (case-ii), the stability analysis predicts that the 8-segment ring has five stable states (i.e., 3-loop to 7-loop states), however, we surprisingly observed six stable states experimentally, in which the 2-loop state was also stable. This may be a result of the contact between different layers. Also, the small corners created at the joints of two adjacent segments in experiments may play a small role in the stability of the segmented ring. In this case, the unstable 1-loop 8-segment ring snaps to a stable 5-loop state once the constraints are released. The stable 5-loop state can either transform into a stable 3-loop state or transition to a stable 7-loop state under single-layer folding. The 2-loop state can fold into the 4-loop state under single-layer folding while transforming into the 6-loop state under double-layer folding. The 6-loop state can also be obtained from the 4-loop state by single-layer folding. The experimental demonstration for the transitions between the six stable states with $\kappa_n L_T/2\pi = 4$ is provided in Movie S5. For $\kappa_n L_T/2\pi = 7$ (case-iii), there are five stable states for the 8-segment ring (i.e., 6-loop to 10-loop states). Starting with the unstable 1-loop state, the 8-segment ring spontaneously snaps to the 7-loop state, and the 7-loop state can invert into the 9-loop state by single-layer folding. Alternatively, the unstable 2-loop state can spontaneously snap to the 6-loop state. The 6-loop state can fold into the 8-loop state through single-layer folding and invert into the 10-loop state through double-layer folding (SI Appendix, Fig. S25 and Movie S6). Interestingly, we

find that such an inversion process for the 8-segment ring (with nonnegative natural curvature) only occurs between two states when the sum of their loop numbers is 8k ($k = 2, 4, \cdots$) (see SI Appendix, Fig. S26 for the inversion transitions between the 7-loop and 9-loop states, and the 15-loop and the 17-loop states). Moreover, the transition between the 8-loop and 10-loop states can be achieved by single-layer folding. The experimental realization for the transitions between the five stable states with $\kappa_{\rm n} L_{\rm T}/2\pi = 7$ is provided in Movie S7. For $\kappa_{\rm n} L_{\rm T}/2\pi = 10$ (case-iv), the 8-segment rod has four stable states (i.e., 9-loop to 12-loop states). Through single-layer folding, the 9-loop state folds into the 11-loop state, and the 10-loop state transitions to the 12-loop state. These findings demonstrate that the natural curvature of the rod segments can be tuned to decide the stable states of the segmented ring, while the applied bending loads decide the transitions between available states.

Conclusions

In summary, we have uncovered the intrinsic multistability of segmented rings consisting of rod segments with the same natural and initial curvatures. All possible planar equilibrium states of segmented rings with different segment numbers were identified by studying their transition behavior under external stimuli over a wide range of relevant natural curvatures through finite element simulations. To guide the rational design of these different states, we developed a general theoretical framework for assessing the elastic stability of segmented rings based on energy variations, from which the natural curvature ranges for the stability of a single state or the mutual stability between different states can be determined. Experiments were conducted to validate the theoretical and numerical results as well as to demonstrate the rational selection of the natural curvature to achieve multistability. We find that a segmented ring with a rectangular cross-section can have up to six distinct planar stable states, three of which are associated with the 1-loop state and three with the 2-loop state, while the stable states having the same basic state can transition between one another under appropriate external stimuli (Movie S5).

The proposed method to enable multistability for segmented rings is powerful in that it applies for arbitrary segment numbers and initial segment curvatures, although, of necessity, only limited cases were presented as design paradigms. Additionally, within the elastic deformation regime, the design method applies across different sizes, ranging from centimeter to meter level. We believe that the study of multistability of these segmented rings can be used to develop reconfigurable metamaterials for tunable properties due to their ability to transition between different stable states. On the other hand, the extreme packing ability and self-guided deployment/folding of these segmented rings hold tremendous application potential in deployable aerospace structures, where the structures need to be packed into a small volume state to facilitate the transportation and then deployed into a large volume state to fulfill certain functionality. These multistable rings can also serve as building blocks to create large ring assemblies for deployable aerospace structures and metamaterials.

Materials and Methods

Fabrication of Segmented Rings. The segmented rings are fabricated using multiple stainless-steel rods with rectangular cross-sections (h = 2 mm and t = 0.5 mm). The rod segment can be manually reshaped by applying plastic deformation to achieve the desired natural curvature. Connections between adjacent rod segments are achieved by plastically deforming a long rod, which introduces small "corners" in the segmented ring. The corners have negligible effects on the overall behavior of the segmented ring when the corner size is small enough. In our experiments, the radius of the corners is roughly 5 mm.

FEA Simulations. Transition behavior of the 1-loop and 2-loop segmented rings under external stimuli are simulated using the commercial software

- D. Melancon, B. Gorissen, C. J. García-Mora, C. Hoberman, K. Bertoldi, Multistable inflatable origami structures at the metre scale. Nature 592, 545-550 (2021).
- A. Zareei, B. Deng, K. Bertoldi, Harnessing transition waves to realize deployable structures. Proc. Natl. Acad. Sci. U.S.A. 117, 4015-4020 (2020).
- Y. Li, S. Pellegrino, A theory for the design of multi-stable morphing structures. J. Mech. Phys. Solids 136, 103772 (2020).
- S. Shan et al., Multistable architected materials for trapping elastic strain energy. Adv. Mater 27, 4296-4301 (2015).
- A. Seyedkanani, A. Akbarzadeh, Magnetically assisted rotationally multistable metamaterials for tunable energy trapping-dissipation. Adv. Funct. Mater. 32, 2207581 (2022).
- H. Fu et al., Morphable 3D mesostructures and microelectronic devices by multistable buckling mechanics. Nat. Mater 17, 268-276 (2018).
- Y. Li et al., Reconfiguration of multistable 3D ferromagnetic mesostructures guided by energy landscape surveys. Extreme Mech. Lett. 48, 101428 (2021).
- S. Wu et al., Stretchable origami robotic arm with omnidirectional bending and twisting. Proc. Natl. Acad. Sci. U.S.A. 118, e2110023118 (2021).
- Y. Chi et al., Bistable and multistable actuators for soft robots: Structures, materials, and functionalities. Adv. Mater 34, 2110384 (2022).
- Y. Li, S. J. Avis, T. Zhang, H. Kusumaatmaja, X. Wang, Tailoring the multistability of origamiinspired, buckled magnetic structures via compression and creasing. Mater. Horizons 8, 3324-3333 (2021).
- 11. F. Qi et al., Defected twisted ring topology for autonomous periodic flip-spin-orbit soft robot. Proc. Natl. Acad. Sci. U.S.A. 121, e2312680121 (2024).
- 12. N. Vasios, B. Deng, B. Gorissen, K. Bertoldi, Universally bistable shells with nonzero Gaussian curvature for two-way transition waves. Nat. Commun. 12, 695 (2021).
- 13. K. Che, C. Yuan, J. Wu, H. Jerry Qi, J. Meaud, Three-dimensional-printed multistable mechanical metamaterials with a deterministic deformation sequence. J. Appl. Mech. 84, 011004 (2017).
- T. Chen, M. Pauly, P. M. Reis, A reprogrammable mechanical metamaterial with stable memory. Nature 589, 386-390 (2021).
- 15. Z. Meng, W. Qin, T. Mei, C. Q. Chen, Bi-material sinusoidal beam-based temperature responsive multistable metamaterials. Int. J. Solids Struct. 277, 112343 (2023).

ABAQUS 2021 (Dassault Systèmes, France) and simulation details are provided in SI Appendix, section S3.

Data, Materials, and Software Availability. All study data are included in the article and/or supporting information.

ACKNOWLEDGMENTS. This work was funded by the NSF Award CPS-2201344 and NSF Career Award CMMI-2145601.

- 16. T. Yu et al., Numerical modeling of static equilibria and bifurcations in bigons and bigon rings. J. Mech. Phys. Solids 152, 104459 (2021).
- L. Lu, J. Dai, S. Leanza, J. W. Hutchinson, R. R. Zhao, Multiple equilibrium states of a curved-sided hexagram: Part II-Transitions between states. J. Mech. Phys. Solids 180, 105407 (2023).
- 18. S. Wu et al., Ring origami: Snap-folding of rings with different geometries. Adv. Intell. Syst. 3, 2100107 (2021).
- 19. S. Wu, J. Dai, S. Leanza, R. R. Zhao, Hexagonal ring origami-Snap-folding with large packing ratio. Extreme Mech. Lett. 53, 101713 (2022).
- 20. J. Dai, L. Lu, S. Leanza, J. Hutchinson, R. R. Zhao, Curved ring origami: Bistable elastic folding for magic pattern reconfigurations. J. Appl. Mech. 90, 121013 (2023).
- L. Lu, S. Leanza, J. Dai, X. Sun, R. R. Zhao, Easy snap-folding of hexagonal ring origami by geometric modifications. J. Mech. Phys. Solids 171, 105142 (2023).
- X. Sun et al., Phase diagram and mechanics of snap-folding of ring origami by twisting. Int. J. Solids Struct. 248, 111685 (2022).
- L. Lu, J. Dai, S. Leanza, R. R. Zhao, J. W. Hutchinson, Multiple equilibrium states of a curved-sided hexagram: Part I-Stability of states. J. Mech. Phys. Solids 180, 105406 (2023).
- T. Yu, F. Marmo, P. Cesarano, S. Adriaenssens, Continuous modeling of creased annuli with tunable bistable and looping behaviors. Proc. Natl. Acad. Sci. U.S.A. 120, e2209048120 (2023).
- C. Shi et al., Morphological transformations of vesicles with confined flexible filaments. Proc. Natl. 25. Acad. Sci. U.S.A. 120, e2300380120 (2023).
- 26. D. Moulton, T. Lessinnes, A. Goriely, Morphoelastic rods. Part I: A single growing elastic rod. J. Mech. Phys. Solids **61**, 398–427 (2013).
- S. Leanza, R. R. Zhao, J. W. Hutchinson, On the elastic stability of folded rings in circular and straight
- states. Eur. J. Mech. Solids 104, 105041 (2024). B. Audoly, K. A. Seffen, Buckling of naturally curved elastic strips: The ribbon model makes a difference. J. Elasticity 119, 293-320 (2015).
- R. S. Manning, K. A. Hoffman, Stability of n-covered circles for elastic rods with constant planar intrinsic curvature. J. Elasticity 62, 1-23 (2001).
- P.-O. Mouthuy, M. Coulombier, T. Pardoen, J.-P. Raskin, A. M. Jonas, Overcurvature describes the buckling and folding of rings from curved origami to foldable tents. Nat. Commun. 3, 1-8 (2012)
- 31. M. Vidulis, Y. Ren, J. Panetta, E. Grinspun, M. Pauly, Computational exploration of multistable elastic knots. ACM Trans. Graphics 42, 1-15 (2023).